

Contact Mechanics of Laser-Textured Surfaces

Correlating Contact Area and Friction

Nikolay Prodanov · Carsten Gachot ·
Andreas Rosenkranz · Frank Mücklich ·
Martin H. Müser

Received: 8 August 2012 / Accepted: 30 October 2012 / Published online: 30 November 2012
© Springer Science+Business Media New York 2012

Abstract We study numerically the contact mechanics of a flat and a curved solid. Each solid bears laser-induced, periodic grooves on its rubbing surface. Our surface topographies produce a similar load and resolution dependence of the true contact area as nominally flat, but randomly rough, self-affine surfaces. However, the contact area of laser-textured solids depends on their relative orientation. The estimated true contact areas correlate with kinetic friction measurements.

Keywords Contact mechanics · Friction · Material treatment effects

1 Introduction

The tribological properties of solids with structured surfaces differ from those of untreated solids. Gears could be seen as an extreme example, where the surfaces of cylinders are modified such that they interlock macroscopically. However, two gear wheels lose their grip when brought out of orientation. Similar behavior occurs at the atomic scale: the friction between two identical crystals can be vanishingly small when they are misaligned, and no contaminants are present at the sliding interface [1–3]. One would certainly

expect related trends at mesoscopic scales, i.e., better interlocking of two solids in contact and thus higher *static* friction between them if their surface corrugation matched on micrometer scales. It is nevertheless not obvious how *kinetic* friction F_k would change, because (geometric) interlocking does not necessarily induce (mechanical) instabilities or enhanced dissipation during sliding [4].

Laser surface texturing (LST) [5] allows one to investigate how kinetic friction is affected by roughness on micrometer scales. LST exploits the interference patterns of nanosecond laser pulses producing texture periods λ_t of a few microns. In detail, a temperature gradient between positions of maximum and minimum laser intensity induces a surface tension gradient, which leads to a transfer of molten material away from the hot spots. A sinusoidal surface topography remains after resolidification.

The tribological properties of laser-textured surfaces often turn out to be improved, which is commonly attributed to their sealing ability and the presence of lubrication pockets [5–7]. However, friction also turns out to be reduced for unlubricated, textured solids as demonstrated by Sung et al. [8], who studied the friction between a “smooth” sphere placed on top of a lithographically structured substrate.

A possible explanation of reduced dry—perhaps even reduced wet—friction between textured surfaces is that the laser-induced corrugation reduces the true contact area A_c as compared to untreated solids. Assuming a local constitutive relation between shear stress τ and normal pressure p of the form

$$\tau = \tau_0 + \mu_0 p, \quad (1)$$

where τ_0 and μ_0 are system-dependent constants, smaller contact area implies smaller friction. The reason is that integrating Eq. (1) over the contact area yields

N. Prodanov · C. Gachot · A. Rosenkranz · F. Mücklich
Department of Materials Science and Engineering, Saarland
University, Campus, 66123 Saarbrücken, Germany
e-mail: c.gachot@mx.uni-saarland.de

N. Prodanov · M. H. Müser (✉)
Jülich Supercomputing Centre, Institute for Advanced
Simulation, FZ Jülich, Jülich, Germany
e-mail: martin.mueser@mx.uni-saarland.de;
m.mueser@fz-juelich.de

$$F_k = \tau_0 A_c + \mu_0 L, \quad (2)$$

where L is the normal load.

Although Eq. (1) has been argued to hold from the macroscopic scale [9] all the way down to the atomic scale [10, 11], its use is not unproblematic. This is because contact is not well defined. In continuum mechanics, the true contact area depends on the resolution of the spatial features [12, 13]. Even when including the smallest, that is, the atomistic features, the precise definition of true contact remains ambiguous, because there is no more clear separation of surface and body forces. As a consequence, τ_0 and μ_0 cannot be uniquely determined. If it were possible to reconcile brave but otherwise disparate attempts of defining contact at the atomic scale [14–17], one would still be faced with the discontinuity of the shear stress in the constitutive Eq. (1). In contrast to continuum descriptions, real interatomic forces are continuous functions of atomic coordinates. For this latter reason, we will remain in the realm of continuum mechanics and treat τ_0 and μ_0 as scale- or resolution-dependent.

Even after restricting ourselves to a scale-dependent interpretation of Eq. (1), one could argue that materials with different λ_t have different values for τ_0 and μ_0 . However, for fixed λ_t , these two numbers should be well defined in the case of dry friction, which allows us to change the contact area at fixed load by changing the orientation.

In this work, we investigate how the contact area of two laser-textured surfaces as well as the contact pressure distribution depend on load and resolution. For this purpose, we present some simple analytical considerations as well as numerical contact mechanics simulations, which are based on experimentally measured height profiles. Finally, we analyze if there is a correlation between (magnification-dependent) contact area and dry friction of laser-textured surfaces.

2 Theory

Most technical surfaces have roughness on wavelengths spanning many decades. Archard recognized that this property makes it difficult to define contact area rigorously [12]. The simplest picture of multi-scale roughness is to have “bumps on a bump,” that is, a clear separation of wavelengths on which roughness lives. Recent tribometer experiments [18] of a ball on a nominally flat substrate, where both surfaces were laser textured, mimic that situation. The ball in these experiments (see also “[Experimental Details](#)” for more details) had a macroscopic radius of curvature of $R_c = 0.75$ mm, while period and amplitude of the laser texturing were $\lambda_t = \mathcal{O}(10 \mu\text{m}) \ll R_c$ and $h_t = \mathcal{O}(1 \mu\text{m})$, leading to a characteristic curvature of $(2\pi/\lambda_t)^2 h_t = \mathcal{O}(1 \mu\text{m}^{-1}) \gg 1/R_c$.

A contact mechanics problem with similar geometry as that of the just-described experiments was analyzed by Yao et al. [19] by finite-element methods. They studied a system with one lateral and one normal direction. The gap of their undeformed surfaces can be written as

$$g(x) = \frac{x^2}{2R_c} + h\{1 - \cos(qx)\}, \quad (3)$$

which corresponds to the set-up of the experiments mentioned above if the two surfaces are perfectly aligned and textured with the same wavelength ($q = 2\pi/\lambda$). The pressure profile had spikes exceeding the values deduced from Hertzian contact mechanics (for $h = 0$), while pressure was zero within most of the contact area, see Fig. 13 in Ref. [19]. However, they did not provide simple guidelines for how to estimate the true area of contact or the pressure distribution. Moreover, they could not consider two surfaces with non-aligned textures, because they only used one lateral dimension. In this section, we describe how to overcome these shortcomings.

In our theoretical approach, we first pursue the idea formalised by Persson [13, 20] of solving the contact mechanics at the coarse scale and of refining the calculations, as spatial features on smaller and smaller wavelengths λ_{res} are resolved. However, it would be naïve to use the original Persson formalism, which necessitates the height spectra to be continuous so that the perceived changes in relative contact area depend continuously on λ_{res} .

The macroscopic geometry is Hertzian. In order to keep the discussion of the local geometry simple and brief, we first restrict our attention to an orthogonal orientation of the (undeformed) laser texture lines. Their gap geometry is that of two crossed cylinders, which can again be described as Hertzian contacts. Moreover, we assume that there is no phase shift between the roughness at the coarse and the fine scales, i.e., we generalize Eq. (3) to

$$g(x, y) = \frac{x^2 + y^2}{2R_c} + h\{2 - \cos(qx) - \cos(qy)\}. \quad (4)$$

Thus, we have a macroscopic surface curvature of R_c and one at the laser-structuring scale of $R_t \approx q^2/2h$. The central “bump on a bump” lies at $\mathbf{r} = (x, y) = 0$, while the “nearest bumps” lie at $(x, y) = (\pm\lambda, 0)$ and $(x, y) = (0, \pm\lambda)$, and the “next-nearest bumps” at $(x, y) = (\pm\lambda, \pm\lambda)$, where $\lambda = 2\pi/q$.

In the macroscopic description of a Hertzian contact, contact radius a and the local pressure $p(r)$ with $r = |\mathbf{r}|$ satisfy

$$a^3 = \frac{3LR}{4E^*}, \quad (5)$$

$$p(r) = p_0 \sqrt{1 - r^2/a^2}, \quad (6)$$

where L is the normal load and $p_0 = 3L/2\pi a^2$ is the maximum interfacial pressure.

Using Eq. (5) one can estimate the load at which the contact radius is as large as the laser texturing wavelength λ , that is, $L_\lambda = 4E^* \lambda^3/3R$. The numerical result for L_λ differs substantially between macroscopic and microscopic curvatures. Using $E^* = \mathcal{O}(100 \text{ GPa})$ and the other values as introduced above, one obtains $L_{c\lambda} = 0.1 \text{ N}$ and $L_{\lambda} = 100 \text{ N}$, respectively. Thus, from a macroscopic perspective, we would need a load of 0.1 N to have not only the central but also the nearest bump in contact. Moreover, within linear elasticity, we can estimate the load where the central contact patch coalesces with the nearest patches to be 100 N. The corresponding values for the interfacial peak pressures are $p_{c0} = \mathcal{O}(1 \text{ GPa})$ and $p_{t0} = \mathcal{O}(10^3 \text{ GPa})$. Given that the hardness of the softer material in our reference experiments [18] is close to 2 GPa, one can conclude that merging contact patches associated with the central and the nearest bump requires pressures exceeding the hardness by two to three orders of magnitude. One is, therefore, safe to assume that this can only happen under major plastic deformation.

One might even conclude that plastic deformation is likely to occur in the central bump before the nearest bumps form contact, see also Fig. 2 in Ref. [18]. This, however, is not the case, because the central bump gets shifted upward more strongly than predicted in the continuum treatment. The depth of indentation $d = a^2/R$ related with the small-scale bump is roughly 1 μm . However, the gap of the undeformed surfaces at $r = \lambda$ is only 1 nm. Thus, the nearest bump must come in contact much earlier than one would assume from continuum mechanics. Using the same equations and parameters as above, one obtains a required load of $L = \mathcal{O}(0.3 \mu\text{N})$, where the small-scale indentation of the central bump reaches an indentation of $\mathcal{O}(1 \text{ nm})$. Therefore, miniscule forces are sufficient to bring the nearest bumps into contact as well.

When trying to bring the next-nearest bumps located at $\lambda (\pm 1, \pm 1)$ into contact, higher forces are needed: now one needs twice the previous displacement, implying that the central bump carries $2^{3/2}$ times the load than before. Moreover, the four nearest bumps (assuming they have identical height) will already carry half the load as the central bump, i.e., bringing the “third shell” into contact requires almost 10 times higher loads or $L = \mathcal{O}(3 \mu\text{N})$ than bringing the second shell into contact. One could easily continue the calculation for the next few shells, but this would not be meaningful, because the real geometry of the small-scale asperities is different from the smooth profiles considered in this toy model. One may yet conclude that (a) miniscule loads suffice to form contact not only in the central bump but also on adjacent bumps, i.e., contact is formed outside the nominal

Hertzian contact area, while inside of it, the real relative contact area is small. (b) The normal load must increase quite dramatically to induce contact in additional shells when the number of shells in contact is small.

In the remainder of this section, we address the question how the contact area changes as a function of the orientation angle α of the grooves. Intuitively, one might expect much larger contacts when the grooves are perfectly aligned, because of line contacts. Once the grooves are brought out of alignment, for instance when oriented at right angles, we are left with a few individual contact patches which have two small spatial dimensions rather than a large one and a small one. We will resort to regular Persson theory to show that this intuition might be misleading.

In Persson theory [13, 20], the pressure distribution broadens approximately by an amount $\Delta p(\mathbf{q})$, which is proportional to the height spectrum at the wavevector that is just being resolved, i.e., for discrete height spectra

$$\Delta p^2(\mathbf{q}) = \left(\frac{qE^*}{2}\right)^2 |\tilde{h}(\mathbf{q})|^2. \tag{7}$$

An increase in the width of the pressure distribution then leads to a reduction in the contact area.

One can now estimate the broadening of the pressure distribution for two different orientations of ridges,

$$h_{\perp}(x, y) = h\{\cos(qx + \Delta\varphi_x) + \cos(qy + \Delta\varphi_y)\}, \tag{8}$$

$$h_{\parallel}(x, y) = h\{\cos(qx + \Delta\varphi_1) + \cos(qx + \Delta\varphi_2)\}, \tag{9}$$

where the various phase shifts $\Delta\varphi$ should be almost uniformly distributed during sliding. The subscripts \perp and \parallel identify perpendicular and parallel orientation, respectively. The corresponding non-zero Fourier coefficients read

$$\tilde{h}_{\perp}(\pm q, 0) = \frac{h}{2} e^{\pm i\varphi_x}, \tag{10}$$

$$\tilde{h}_{\perp}(0, \pm q) = \frac{h}{2} e^{\pm i\varphi_y}, \tag{11}$$

$$\tilde{h}_{\parallel}(\pm q, 0) = \frac{h}{2} (e^{\pm i\varphi_1} + e^{\pm i\varphi_2}). \tag{12}$$

Squaring the individual contributions and taking their expectation values by sampling all phases $\Delta\varphi$ with equal probability then yields that both orientations of the grooves lead to the same pressure distribution broadening of

$$\Delta p^2_{\perp, \parallel} = \left(\frac{qhE^*}{2}\right)^2 \tag{13}$$

independent of the relative orientation. This result implies similar contact areas in both cases.

As mentioned above, Persson theory cannot be expected to give quantitative answers when height spectra have

pronounced peaks. However, the current calculation reveals that the effect of orientation might be small. A more reliable quantitative assessment is made in “Results” section.

3 Methods

3.1 Experimental Details

In this section, we sketch the relevant details of the experiments providing us with the surface roughness measurements and the mechanical properties of the two solids in contact. For a more complete list of details, we refer to the original publication [18].

In the experiments, a commercially available austenitic stainless steel (1.4301) was used as substrate material with a typical yield strength ranging between 360 and 680 MPa. Its hardness, as determined by nanoindentation, is approximately 2.2 GPa and the effective elastic modulus is 167 GPa [21]. The lateral dimensions of the nominally flat specimens are 20×20 mm. The samples were delivered with a highly polished mirror-like surface finish having a root-mean-square roughness of about 30 nm. The counter body consists of a 100Cr6 steel bearing ball with a diameter of 1.5 mm. Effective elastic modulus and yield strength are 140 and 1.4 GPa, respectively [21].

A pulsed Nd:YAG laser (Spectra Physics, Quanta Ray PRO 290) with a pulse duration of 10 ns was used for the laser patterning. The laser fluence was set to 400 mJ/cm^2 for all specimens. The periodicity (line-spacing) analyzed in this work are 9 and $18 \mu\text{m}$. The topography was measured using a white light interferometer WLI (Zygo New View 100) equipped with a 3D imaging surface structure analyzer. This is an established method of characterizing surfaces in a fast non-contact mode. The vertical resolution is typically in the range of sub-nanometer and the lateral resolution up to the Rayleigh limit (usually $0.5 \mu\text{m}$) [22]. It is noteworthy that surface errors such as ghost steps or spikes may appear due to an identification problem of the fringe order thus leading to the so-called 2π -jumps for textured surfaces [22].

3.2 Smoothing Surface Data

To a very good approximation, the true contact area of regular solids with self-affine surface topography is inversely proportional to the root-mean-square gradient of the gap between the undeformed surfaces. Since roughness tends to live predominantly at the smallest scales, short-range fluctuations of the height, which are the most susceptible to experimental errors, determine what contact area is predicted for a measured height topography. In most

cases, it will, therefore, be necessary to post-process and to smooth experimentally determined surface heights. Moreover, smoothing helps one to rationalize results in terms of Persson theory, which is based on analyzing contacts at different “magnifications.” Specifically, smoothing over a large domain corresponds to small resolution or small magnification.

In this work, we analyze how various smoothing operations on surface topographies affect our data of interest. Two common techniques are investigated, namely Gaussian filtering and Fourier smoothing. In Gaussian filtering, the smoothed height profile is given by

$$h_{\text{Gauss}}(\mathbf{r}) = \frac{1}{2\pi\sigma^2} \int d^2r' h(\mathbf{r}') \exp\left\{-\frac{(\mathbf{r}-\mathbf{r}')^2}{2\sigma^2}\right\}, \quad (14)$$

where σ is a measure of the spatial resolution. When smoothed in Fourier space, the original height spectrum is Fourier transformed. All Fourier coefficients $\tilde{h}(\mathbf{q})$ with a wavelength $\lambda < 2\pi/q$ are set to zero and the remaining coefficients are transformed back to real space. The effect of the two smoothing filters are shown in Fig. 1.

At locations where height profiles are repetitive and do not suffer from erratic measurement errors, the Fourier filtering reproduces more clearly that the tops of asperities are flattened. However, in the vicinity of errors, or nearby steep gradients, we found the local Gaussian filters to be advantageous, because Fourier leads to ringing near sharp corners. It is also noteworthy that the worn surfaces can be described very accurately as sinusoidal with cut-off caps. We, therefore, believe that the highest point of the hard

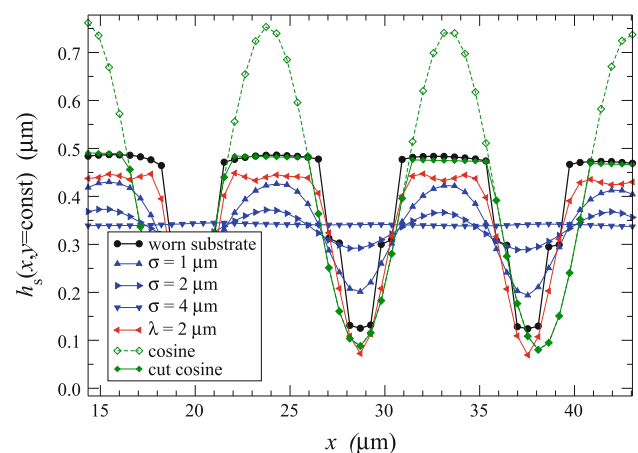


Fig. 1 Surface height of a substrate along a selected scan line. The experimental data of a worn laser-textured surface are shown in *black circles*. Gaussian filter with *blue triangles* representing resolutions $\sigma = 1 \mu\text{m}$ (*triangle up*), $2 \mu\text{m}$ (*triangle right*), and $4 \mu\text{m}$ (*triangle down*), and Fourier smoothing with resolution $\lambda = 2 \mu\text{m}$ (*red triangle left*). The *green diamonds* indicate a simple cosine profile of a $9.7 \mu\text{m}$ wavelength (*open diamonds*) and a cosine profile which is cut at a specified height (*closed diamonds*)

counterface (at a given scan line) determines the resulting asperity height of the substrate.

3.3 Computational Method

For our calculations, we use the Green's function molecular dynamics method (GFMD) [23] as described in Ref. [24]. Specifically, we use the small-slope approximation, which allows one to map elasticity and roughness to one side of the interface and to reduce the deformation to a scalar. The elastic energy then reads

$$E = \frac{E^*}{4} \sum_{\mathbf{q}} q |\tilde{u}(\mathbf{q})|^2, \quad (15)$$

where the in-plane wave vector \mathbf{q} is always chosen such that $-\pi/\mathcal{L} \leq q_x < \pi/\mathcal{L}$, where \mathcal{L} is the linear dimension of the contact. Dynamics are integrated in reciprocal space, i.e., we solve the equation of motion for the Fourier transforms of the displacements $\tilde{u}(\mathbf{q})$:

$$m\ddot{u}(\mathbf{q}, t) + m\gamma\dot{u}(\mathbf{q}, t) + \frac{qE^*}{2}\tilde{u}(\mathbf{q}, t) = -p\delta_{0\mathbf{q}}, \quad (16)$$

where m is an inertia and γ reflects an inverse damping time. The externally imposed pressure p is supposed to only live on a zero wavelength as indicated with the Kronecker δ symbol. When the interaction between the two surfaces is expressed as a continuous force, it is possible to choose m and γ as a function of \mathbf{q} . However, we use non-holonomic boundary conditions of the form

$$u(\mathbf{r}) + g(\mathbf{r}) \geq 0, \quad (17)$$

where $g(\mathbf{r})$ is the gap between the original surfaces before they touch, in which case m and γ may not depend on \mathbf{q} .

The smallest wavenumber in the system is associated with the mode having the largest wavelength. Since the stiffness of the displacement is proportional to q , a reduction of the smallest frequency scaling with $\sqrt{\pi/\mathcal{L}}$ seems unavoidable. In order to reach fast convergence, the damping should be chosen such that the slowest mode, i.e., the center of mass motion, is close to being critically damped, which can be recognized particularly well when the center-of-mass mode is slightly underdamped. Since the stiffness of the contact grows roughly proportional with the normal pressure [25, 26], the optimum choice for damping satisfies $\gamma \propto \sqrt{p/\mathcal{L}}$. In this case, the number of GFMD time steps required to reach convergence only grows with $\sqrt{\mathcal{L}}$ independent of pressure. Refinement of this procedure are only needed when the relative contact area is much less or close to one, e.g., $A_r < 10^{-3}$, or $1 - A_r < 10^{-3}$.

For the integration of motion, we employ the standard Verlet algorithm. The boundary conditions are imposed

after new positions are determined. Specifically, we set $u(\mathbf{r}) = -g(\mathbf{r})$ if $u(\mathbf{r})$ was predicted to be smaller than $-g(\mathbf{r})$.

4 Results

Before the computing contact area as a function of load, resolution, and orientation, it is instructive to analyze the effect of the smoothing operations on the contact patch geometry first. In Fig. 2, contacts are shown in real space for the various smoothing procedures presented before in Fig. 1. In these calculations, we have increased the load by a factor of 100 with respect to the reference experiments, because those loads are much too small to allow for a meaningful visualization. Moreover, the trends do not depend sensitively on the precise value of the load.

When smoothing surfaces with Gaussian filters (shown in the left part of Fig. 2), one can recognize that the contact area increases with decreasing resolution, which is proportional to $1/\sigma$. However, it is also noticeable that the contact area for the larger resolution, or small σ , is more spread out than for the smaller resolution. This confirms the picture laid out in “Theory.” The $\sigma = 4 \mu\text{m}$ surfaces produce a single, connected domain, almost reminiscent of a circular Hertzian contact. Conversely, the highest resolution, i.e., $\sigma = 1 \mu\text{m}$, has contact at larger radii although its total contact area is relatively small. The reason is that the normal displacement is accommodated by the small-scale asperities at high resolution.

When smoothing surfaces with Fourier filters, the contact looks more erratic than in the other cases, which is shown in the right part of Fig. 2. We attribute this observation to the fact that the Fourier smoothing is less forgiving to experimental uncertainties than the Gaussian

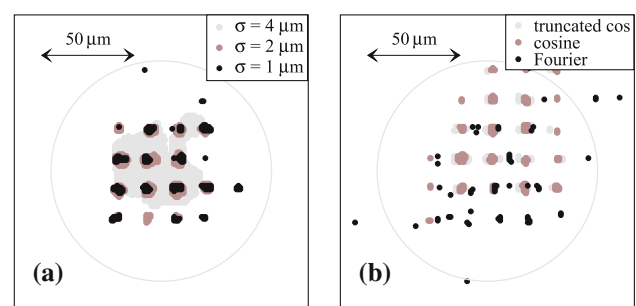


Fig. 2 Elastic contact for a worn $\lambda_t = 9 \mu\text{m}$ surface at 100 times the experimental load for different smoothing operations. **a** Gaussian filter (applied to both surfaces) with $\sigma = 4 \mu\text{m}$ (light gray), $2 \mu\text{m}$ (brown), and $1 \mu\text{m}$ (black). **b** Surfaces in which the substrate topography is a truncated cosine (light gray), simple cosine (brown), and a Fourier filter with $\lambda = 2 \mu\text{m}$. The counterface consists of a hard 100Cr6 bearing steel ball, smoothed with a Gaussian filter of $\sigma = 2 \mu\text{m}$. The gray circles are drawn to guide the eye

smoothing. However, surprisingly small differences in the contacts are found for the truncated cosine and the original cosine data. The features observed in both cases are similar to those revealed in the Gaussian smoothing.

While we have focused so far on the orthogonal orientation of the texture lines, our interest lies in correlating friction and contact area, which both depend on the relative alignment of the two surfaces. In this context, it is worth pointing out that parallel grooves have larger fluctuations than orthogonal grooves. This is demonstrated in Fig. 3.

The results shown in Fig. 3 can be easily rationalized. At mesoscopic scales, where spatial features are resolved to roughly the laser texturing wavelengths but not much beyond, all configurations with an alignment of 90° are equivalent if sliding occurs parallel to the grooves of one of the two surfaces. One would, therefore, expect small variations with slid distance. Conversely, when the grooves are aligned, and the surfaces are slid in a right angle to the texturing, the extreme configurations would be that peaks on one surface face the peaks on the other surface or that peaks are opposite to valleys.

If more features at smaller scales are resolved, the sensitivity of the relative contact area with orientation decreases. This is because local contact can be interpreted as the contact between two rough surfaces. In the extreme case, i.e., when resolving roughness down to the atomic scale, true contact area will, as usual, be miniscule. The question arises if roughness on wavelengths close to λ_t still matters. As discussed above, contact area (for unstructured surfaces) is roughly inversely proportional to the root-mean square slope. The contribution of each wave vector is proportional to the mean square gradient, which is $g^2 = q^2 \langle |\tilde{h}(\mathbf{q})|^2 \rangle$. For the simple sinusoidal surface profiles shown in Fig. 1 with a height variation of $\Delta h(\lambda_t) \approx 1.2 \mu\text{m}$ at $\lambda_t \approx 18 \mu\text{m}$, one obtains a value for $g = (2\pi \cdot \Delta h/\lambda)^2/2 = \mathcal{O}(0.1)$. This constitutes a non-negligible contribution to the overall roughness. Thus, one will probably have to go to very high resolution before height fluctuations at much smaller scales than λ_t start to be relevant.

In Fig. 4, we show the estimated contact area as a function of load for the $\lambda_t = 9 \mu\text{m}$ surfaces with parallel and orthogonal alignment after smoothing with a $\sigma = 2 \mu\text{m}$ Gaussian filter. One can see that the area scales well with $L^{0.9}$, which is half way between the standard $A_{\text{real}} \propto L$ and Archard's $A_{\text{real}} \propto L^{4/5}$ prediction for a system similar to ours [12]. In the regime where error bars are small, we find that the contact area in an interface with parallel grooves is 4/3 times larger than that with orthogonal grooves. However, it is remarkable that at the smaller scales, we would predict a mean pressure of $1 \text{ mN}/2 \mu\text{m}^2 = 0.5 \text{ GPa}$, which is already one fourth of the

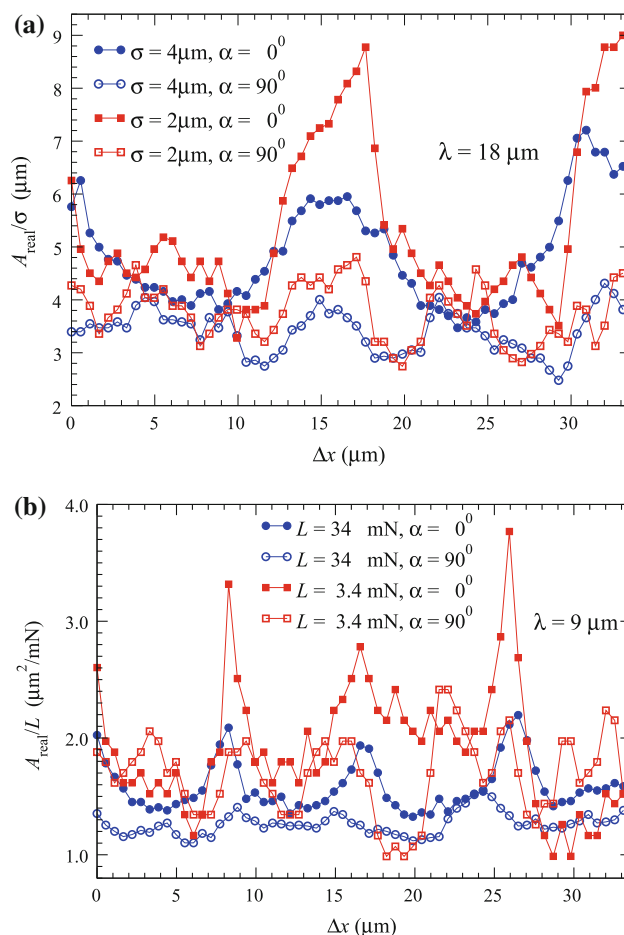


Fig. 3 **a** Real contact area A_{real} divided by the resolution σ and **b** A_{real} divided by load L as function of the lateral shift Δx . Surfaces are smoothed with Gaussian filters having resolution $\sigma = 4 \mu\text{m}$ (blue circles) and $\sigma = 2 \mu\text{m}$ (red squares). Closed and open symbols indicate parallel and orthogonal grooves, respectively. The calculations are conducted for **a** an unworn $\lambda_t = 18 \mu\text{m}$ and **b** a worn $\lambda_t = 9 \mu\text{m}$ surface

macroscopic hardness of the substrate. This means that the tail of the pressure distribution easily exceeds the hardness of the substrate. Consequently, one should expect some plastic deformation of the surfaces, in particular when they are in relative sliding motion.

Finally, we wish to note that the pressure probability distribution inside our contacts does not change significantly over a broad range in normal forces, i.e., from 4 to 512 mN, except that a small load implies large stochastic scatter, see Fig. 5. Likewise, the relative orientation of the surfaces does not appear to matter much either for the pressure distribution. However, once the resolution changes, the pressure distribution changes in a quite remarkable way. This is precisely the behavior, which one would expect from Persson theory for randomly rough surfaces [13, 20].

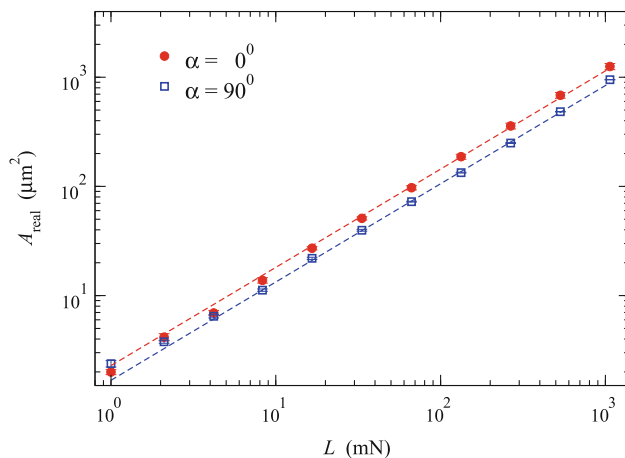


Fig. 4 Estimated real contact area A_{real} as a function of load for two different orientations of $\lambda_t = 9 \mu\text{m}$ surfaces: $\alpha = 0^\circ$ (closed red circles) and $\alpha = 90^\circ$ (open blue squares). Broken lines reflect fits with $A_{\text{real}} \propto L^{0.9}$. The prefactor for $\alpha = 0^\circ$ is 4/3 times larger than that for $\alpha = 90^\circ$. The height topography are smoothed with a Gaussian filter of $\alpha = 2 \mu\text{m}$. Averages were taken over 10 periods

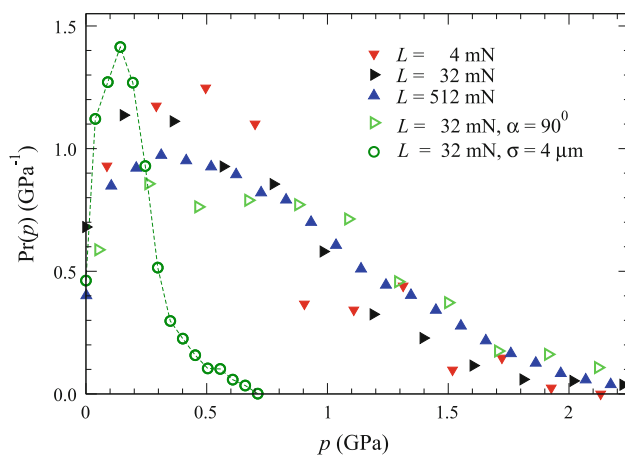


Fig. 5 Pressure probability distribution function $\text{Pr}(p)$ for different loads, orientations, and smoothing. Default values are load $L = 32 \text{ mN}$, $\alpha = 0^\circ$, and $\sigma = 2 \mu\text{m}$ as reflected by the green right triangles. Loads of 4 and 512 mN are indicated by red down and blue up triangles, respectively. One calculation is based on an orthogonal orientation of $\alpha = 90^\circ$, see the green open right triangles and one calculation is based on a different smoothing with $\alpha = 4 \mu\text{m}$, which is indicated with green open circles. The function values of the last dataset has been divided by three

Previous atomistic simulations of amorphous, single-asperity tips had already revealed that the pressure-distribution evaluated at the smallest scales may deviate strongly from that obtained for a Hertzian tip in the continuum limit [14, 15]. In this sense, our results are not surprising.

Yet, what might be unexpected is that the pressure distribution has some remaining weight at values near the estimated substrate hardness of nanoindentation of 2.2 GPa. This weight would raise substantially if we increased

our resolution. Unexpectedly large contact pressures have also been identified in a recent discrete-dislocation simulation of a rigid platen pressing against a sinusoidal aluminum surface [27].

5 Discussion and Conclusions

In this study, experimentally determined height profiles of laser-textured steel surfaces are used in a computer simulation addressing the question how the real contact area A_{real} depends on the relative orientation α of the laser-induced grooves. For the given surfaces, it turns out to be very challenging to determine good estimates for the contact area, because it is sensitive to the spatial resolution with which the surfaces are represented. Unfortunately, the smallest scales, where experimental uncertainties are the largest, are the most relevant for the calculation of contact area. However, it turns out that the ratio $A_{\text{real}}(\alpha = 90^\circ)/A_{\text{real}}(\alpha = 0^\circ) \approx 3/4$ is relatively insensitive to the precise choice of load and the smoothing operation.

The experimental differences observed for the kinetic friction F_k are slightly larger, but similar in magnitude, as those for the relative contact area, i.e., $1/3 \gtrsim \{F_k(90^\circ) - F_k(0^\circ)\}/F_k(0^\circ) \gtrsim 1/4$. The interpretation of this result in terms of Eq. (1) is that the “offset term” τ_0 dominates, that is, dissipation in these systems is essentially proportional to the contact area. A possible explanation is that the dissipation mechanism is predominantly plastic deformation, the more so as the deduced shear stress ($\tau = F_k/A \approx 0.025 \text{ mN} / 2 \mu\text{m}^2$) is already roughly a quarter of the yield of the substrate, although we are not yet at the full resolution.

For the remaining values of λ_t , the experimental ratios for the friction were similar as those for $9 \mu\text{m}$. However, due to the lack of surface topographies after rubbing, we have not been in a position to post-analyze the data in the same fashion as we did for the $\lambda_t = 9 \mu\text{m}$ surface. Unfortunately, this also prevented us from conducting a meaningful comparison for similarly aligned surfaces with different laser-texturing period. However, in this context, a result obtained by Sun et al. [27] is worth mentioning. In their study of plastic deformation of solids (aluminum) with an initially sinusoidal surface pressed against a flat, rigid platen, they found that longer periods lead to a larger contact area. Thus, we expect the worn $\lambda_t = 18 \mu\text{m}$ surfaces to have larger contact area than the ones with $\lambda_t = 9 \mu\text{m}$, which would again correlate, at least qualitatively, with friction measurements.

An interesting side aspect of our analysis is the realization that increasing the resolution of the surfaces does not simply lead to the disappearance of local contact area. Instead, sometimes new, small contact patches can be observed at

locations that had been completely out of contact in the calculation on the coarser scale. This observation, which we rationalized in a rather simple “two-scale Hertzian bump-on-a-bump” approach, might be partly responsible for the slight underestimation of contact area in Persson theory [28–30]. This insight might motivate attempts to introduce “reen-trance correction” into the theory.

Acknowledgments N.P. and M.H.M. are grateful for computing time on JUROPA at the FZ Jülich Supercomputing Centre. MHM acknowledges support from the German Research Foundation (DFG) through grant Mu 1694/5-1.

References

- Shinjo, K., Hirano, M.: Dynamics of friction: superlubric state. *Surf. Sci.* **283**, 473–478 (1993)
- Müser, M.H., Wenning, L., Robbins, M.O.: Simple microscopic theory of Amontons’ laws for static friction. *Phys. Rev. Lett.* **86**, 1295–1298 (2001)
- Dienwiebel, M., Verhoeven, G.S., Pradeep, N., Frenken, J.W.M., Heimberg, J.A., Zandbergen, H.W.: Superlubricity of graphite. *Phys. Rev. Lett.* **92**, Article No. 126101 (2004)
- Müser, M.H., Urbakh, M., Robbins, M.O.: Statistical mechanics of static and low-velocity kinetic friction. *Adv. Chem. Phys.* **126**, 187–272 (2003)
- Etsion, I.: State of the art in laser surface texturing. *J. Tribol.* **127**, 248–253 (2005)
- Pettersson, U., Jacobson, S.: Influence of surface texture on boundary lubricated sliding contacts. *Tribol. Int.* **36**, 857–864 (2003)
- Rapoport, L., Moshkovich, A., Perilyev, V., Lapsker, I., Halperin, G., Itovich, Y., Etsion, I.: Friction and wear of MoS(2) films on laser textured steel surfaces. *Surf. Coat. Technol.* **202**, 3332–3340 (2008)
- Sung, I.H., Lee, H.S., Kim, D.E.: Effect of surface topography on the frictional behavior at the micro/nano-scale. *Wear* **254**, 1019–1031 (2003)
- Bowden, F.P., Tabor, D.: *Friction and lubrication*. Wiley, New York (1956)
- Berman, A., Drummond, C., Israelachvili, J.N.: Amontons’ law at the molecular level. *Tribol. Lett.* **4**, 95–101 (1998)
- He, G., Müser, M.H., Robbins, M.O.: Adsorbed layers and the origin of static friction. *Science* **284**, 1650–1652 (1999)
- Archard, J.F.: Contact and rubbing of flat surfaces. *J. Appl. Phys.* **24**, 981–988 (1953)
- Persson, B.N.J.: Theory of rubber friction and contact mechanics. *J. Chem. Phys.* **115**, 3840–3861 (2001)
- Luan, B.Q., Robbins, M.O.: The breakdown of continuum models for mechanical contacts. *Nature* **435**, 929–932 (2005)
- Mo, Y.F., Turner, K.T., Szlufarska, I.: Friction laws at the nanoscale. *Nature* **457**, 1116–1119 (2009)
- Shengfeng, C., Robbins, M.O.: Defining contact at the atomic scale. *Tribol. Lett.* **39**, 329–348 (2010)
- Eder, S., Vernes, A., Vorlaufer, G., Betz, G.: Molecular dynamics simulations of mixed lubrication with smooth particle post-processing. *J. Phys. Condens. Matter* **23**, Article No. 175004 (2011)
- Gachot, C., Rosenkranz, A., Reinert, L., Ramos-Moore, E., Souza, N., Müser, M.H., Mücklich, F.: Dry friction between laser-patterned surfaces: role of alignment, structural wavelength and surface chemistry. *Tribol. Lett.* doi:10.1007/s11249-012-0057-y
- Yao, Y., Schlesinger, M., Drake, G.W.F.: A multiscale finite-element method for solving rough-surface elasticcontact problems. *Can. J. Phys.* **82**, 679–699 (2004)
- Persson, B.N.J.: Contact mechanics for randomly rough surfaces. *Surf. Sci. Rep.* **61**, 201–227 (2006)
- Carvill, J.: *Mechanical Engineers Data Handbook I*. Butterworth-Heinemann, Oxford (1993)
- Gao, F., Leach, R., Petzing, J., Coupland, J.: Surface measurement errors using commercial scanning white light interferometers. *Meas. Sci. Technol.* **19**, Article No. 015303 (2008)
- Campañá, C., Müser, M.H.: Practical Green’s function approach to the simulation of elastic semi-infinite solids. *Phys. Rev. B* **74**, Article No. 075420 (2006)
- Dapp, W.B., Lücke, A., Persson, B.N.J., Müser, M.H.: Self-affine elastic contacts: percolation and leakage. *Phys. Rev. Lett.* **108**, Article No. 244301 (2012)
- Persson, B.N.J.: Relation between interfacial separation and load: a general theory of contact mechanics. *Phys. Rev. Lett.* **99**, Article No. 125502 (2007)
- Campañá, C., Persson, B.N.J., Müser, M.H.: Transverse and normal interfacial stiffness of solids with randomly rough surfaces. *J. Phys. Condens. Matter* **23**, Article No. 085001 (2011)
- Sun, F., Van der Giessen, E., Nicola, L.: Plastic flattening of a sinusoidal metal surface: a discrete dislocation plasticity study. *Wear* **296**, 672–680 (2012)
- Hyun, S., Pei, L., Molinari, J.F., Robbins, M.O.: Finite-element analysis of contact between elastic self-affine surfaces. *Phys. Rev. E* **70**, Article No. 026117 (2004)
- Campañá, C., Müser, M.H.: Contact mechanics of real vs. randomly rough surfaces: a Green’s function molecular dynamics study. *Europhys. Lett.* **77**, 38005–38007 (2007)
- Putignano, C., Afferrante, L., Carbone, G., Demelio, G.: The influence of the statistical properties of self-affine surfaces in elastic contacts: a numerical investigation. *J. Mech. Phys. Solids* **60**, 973–982 (2012)